Nanotechnology

Simultaneous quantification of Young's modulus and dispersion forces with nanoscale spatial resolution

To cite this article before publication: Clodomiro Cafolla *et al* 2023 *Nanotechnology* in press https://doi.org/10.1088/1361-6528/acf8ce

Simultaneous quantification of Young's modulus and dispersion forces with nanoscale spatial resolution

Clodomiro Cafolla[1]*, Kislon Voitchovsky[1], Amir Farokh Payam[2]*

[1]Physics Department, Durham University, Durham, DH1 3LE, UK

[2]Nanotechnology and Integrated Bioengineering Centre (NIBEC), School of Engineering, Ulster University, Newtownabbey BT37 0QB, UK.

*corresponding authors: clodomiro.cafolla@durham.ac.uk; a.farokh-payam@ulster.ac.uk

Abstract

Many advances in polymers and layered materials rely on a precise understanding of the local interactions between adjacent molecular or atomic layers. Quantifying dispersion forces at the nanoscale is particularly challenging with existing methods often time consuming, destructive, relying on surface averaging or requiring bespoke equipment. Here, we present a non-invasive method able to quantify the local mechanical and dispersion properties of a given sample with nanometer lateral precision. The method, based on atomic force microscopy (AFM), uses the frequency shift of a vibrating AFM cantilever in combination with established contact mechanics models to simultaneously derive the Hamaker constant and the effective Young's modulus at a given sample location. The derived Hamaker constant and Young's modulus represent an average over a small (typically <100) molecules or atoms. The oscillation amplitude of the vibrating AFM probe is used to select the length-scale of the features to analyse, with small vibrations able to resolve the contribution of sub-nanometric defects and large ones exploring effectively homogeneous areas. The accuracy of the method is validated on a range of 2D materials in air and water as well as polymer thin films. We also provide the first experimental measurements of the Hamaker constant of HBN, MoT_2, WSe_2 and polymer

films, verifying theoretical predictions and computer simulations. The simplicity and robustness of the method, implemented with a commercial AFM, may support a broad range of technological applications in the growing field of polymers and nanostructured materials where a fine control of the van der Waals interactions is crucial to tune their properties.

Introduction

Quantification of the physical and chemical properties of interfaces at the nanoscale is of crucial importance in the development of new materials with tailored features[1–5]. This is, for example, the case for two-dimensional (2D) materials and van der Waals (vdW) heterogenous structures where a molecular-level understanding of the interactions at play is key to achieve the desired physical, chemical and electronic properties[4–8]. With building units as thin as a single atomic layer, 2D materials tend to exhibit properties dissimilar from their bulk counterpart and can be dramatically influenced by any interactions with a contacting material[1,9]. These unique features open a wealth of opportunities for new generation of electronic devices, combining direct access to high mobility charge carriers and high thermal conductivity[1]. A plethora of exciting properties further arises when combining 2D materials in a single stack or when depositing them on different substrates[1,10,11]. Examples range from extending the plasmonic response of devices in the visible range[12] to developing ferromagnetic semiconductors[10,12] and superlubricity in tribology and lubrication[13].

Fabricating these new 2D materials by design is however challenging[1,14,15]. Undesired structural defects can detrimentally alter the electronic and nanomechanical properties of 2D materials: wrinkles and ripples in mechanically exfoliated MoS_2, or graphene nanobubbles can modify the carrier concentration[16]. Alongside chemical and physical singularities, the other limiting factor in the effective design of 2D materials is the difficulty to fine control the interfacial interactions between each layer, and with the substrate[17]. The structure and properties of a given 2D device typically depend on a balance between vdW adhesion forces and the material's bending energy. In MoS_2, for example, interfacial defects lead to an increase in tensile strain with an associated transition from direct to indirect bandgap[16]. Practically, the most relevant parameters to measure are arguably the Hamaker constant, *H,* which quantifies the magnitude of vdW interactions between the two materials, and the Young's modulus, *E*, which describes the linear elastic response of the sample under strain.[18] The problem goes beyond the characterisation of 2D materials: the engineering of new polymeric materials and thin films, for example, also requires quantification of spatial variations in the *H* and E to correlate molecular changes in morphology with the resulting application performance[19,20]. This is perhaps best illustrated by a technological example: polymeric multilayer thin films for coatings where their lifetime and toxicity depends on crystallisation processes due to dispersive forces[21]. Below a critical thickness around 10 nm, vdW forces between the two adjacent

polymeric layers become dominant over the stabilizing mechanical and capillary forces and they may thus amplify any interfacial instability eventually leading to the layer breakup[22]. The ability to quantify the cohesive dispersion forces and the material's mechanical properties *in-situ* and with nanometric spatial resolution is therefore of paramount importance.

The simultaneous determination of both *H* and *E* while considering local defects is however challenging. Theoretical approaches such as DFT calculations tend to assume idealised defects or simply defect-free interfaces[16,23]. Experimental approaches present also some limitations, in particular when determining *H*. *E* can be indeed studied by nanoindentation[24,25] or atomic force microscopy (AFM) methods[25–27] with nanoscale spatial resolution. AFM, in particular, is an ideal candidate to directly compare topographical features with specific properties such as nanomechanical variations[28–31]. AFM enables mapping the topography of interfaces with sub-nanometer precision while simultaneously quantifying certain physical or chemical properties of the sample, thanks to its reliance on a nanoscale physical probe[32–36]. AFM operational modes are generally divided into static and dynamic, depending on whether the AFM cantilever is kept static at its base, or whether a periodic motion is imposed to it[37]. In most modern studies, the AFM is operated dynamically, with the probe externally vibrated to enhance sensing accuracy while better preserving the tip and the sample[28,29,33,34,37–39]. By tracking changes in the tip vibration frequency, amplitude and phase as it operates in close vicinity to a given sample, it is possible to reconstruct the local interaction force experienced by the tip near the sample's surface. For instance, dynamic AFM methods have been recently applied to soft and hard materials with their mechanical modulus and viscoelastic properties identified with great accuracy[27,40]. In both static and dynamic modes, the contact between the tip and the sample can be described using the classical Hertz model for the case of a sphere in contact with an elastic half space[18,27,41]. The Hertz model is based on the assumptions of a frictionless and non-adhesive contact with the contact area significantly smaller than the radius of the sphere and with the deformation of both surfaces being perfectly reversible[18,27]. Notably, the model assumptions may fall short in the plastic regime, or in the presence of non-negligible adhesive interactions between the AFM probe and the sample. In these cases, the Johnson-Kendall-Roberts (JKR) and the Derjaguin-Muller-Toporov (DMT) models offer a robust description of the interactions between the probe and a compliant or stiff substrate, respectively[18,27].

Considering the determination of *H,* a wide range of experimental techniques have been applied from surface force apparatus[42] and immersion calorimetry[43] to optical techniques, such as dynamic light scattering[44] and ellipsometry[45]. These techniques however tend to be invasive[43]

or average either over multiple locations or large areas[42–44,46]. Also here, AFM has emerged as an ideal tool. For instance, using AFM static modes, the probe is moved laterally along the sample with vdW interactions reconstructed from friction-velocity curves and the activation energy necessary for the tip to start its motion over the substrate[47]. Static AFM modes offer the opportunity to reconstruct vdW interactions also studying the so-called jump-into-contact, that is, an instability in the cantilever motion due to the attractive force gradient being markedly greater than the cantilever spring constant[46]. Existing dynamic AFM however appear superior in comparison to static modes: they are minimally invasive and offer an excellent degree of control when studying single molecules adsorbed on a substrate[8,9]. Still, existing AFM dynamic modes for the study of vdW interactions require specifically functionalised probes[8,9,48] and/or specialist equipment operating at ultrahigh vacuum and in some cases also at low temperatures (5 K). This makes deriving local, nanoscale information often challenging.

To overcome these difficulties, we have developed a novel approach based on AFM where measurements can be conducted using standard commercial equipment operated in air or liquid. Here, we also address the problem of force reconstruction from AFM observables. Force reconstruction is challenging[39,49,50] because it usually relies on multiple deconvolution integrals to capture the multi-harmonic response of the vibrating cantilever to varying tip-sample interactions[51]. Several numerical methods have been developed[51] using slow time varying theory[49], iterative calculations[52] inversions of matrices[53], infinite summations of higher order derivatives[54], and Chebyshev polynomial expansions[55]. These approaches are typically heavy calculations and often only valid for cantilever oscillation amplitudes significantly differing from the length scale of the interaction being probed[51]. The most popular method -the Sader and Jarvis method- provides a good approximation of the interaction forces while still using relatively simple integrals[39,50,51], but still requires the tip oscillation amplitude to be much smaller than the decay length of the interaction at play[51]. While not a problem in itself, this renders any direct quantification of H and E challenging, with most existing studies focusing on solvation effects (see e.g. reviews [56,57]).

Here, using a development based on the viral equation, we derive an analytical expression that relates H and E to quantities directly observable in AFM measurements. This is rendered possible by combining the virial theorem with the DMT model (see e.g. ref.[58] for a detailed review). The method can be easily implemented without the need of any specialized equipment and yields correct values using the standard dynamic operation conditions of commercial AFMs. The method is robust and can be used in both air and liquid, and with a wide range of

oscillation amplitudes thus allowing for quantification across any desired length scale. For example, we use it to investigate the impact of nanoscale singularities and roughness on the derived quantities. We compare the results of the proposed method against literature values over a range of samples including some 2D and polymeric materials. We also run simulations verifying the experimental measurements. The proposed method offers a robust and non-invasive approach to accurately study mechanical properties and, above all, vdW interactions with high accuracy and spatial precision paving the way for efficiently designing of 2D heterostructures and new polymeric materials.

Results and discussion

The AFM is firstly operated in amplitude modulation (AM) to image the sample surface and highlight any nanoscale topographical defects or singularities (Fig. 1a). In this mode, the cantilever is driven with a constant oscillation amplitude and frequency with the changes in the former being used to re-construct the sample topography[33,36,37].

The nano-positioning system of the AFM allows selecting the nanoscale region of interest to probe by AFM force spectroscopy. Force spectroscopy is conducted in frequency modulation (FM) to allow straightforward separation of the dissipative and conservative forces experienced by the tip (Fig. 1a)[37]. In FM mode, the driving frequency is adjusted to always match the resonance frequency of the cantilever using a feedback loop that also ensures a 90° phase shift between the driving and tip oscillations. An additional feedback keeps the tip oscillation amplitude constant[37,59].

Force spectroscopy measurements quantify the frequency shift, Δf, in the tip oscillation as it approaches the surface of the sample, yielding the characteristic frequency-distance (FD) curves where Δf is shown as a function of the tip-sample distance, d (Fig. 1). From FD curves, it is possible to extract the position a_0 of the transition from the attractive to repulsive region of the force experienced by the tip as it moves towards the surface.

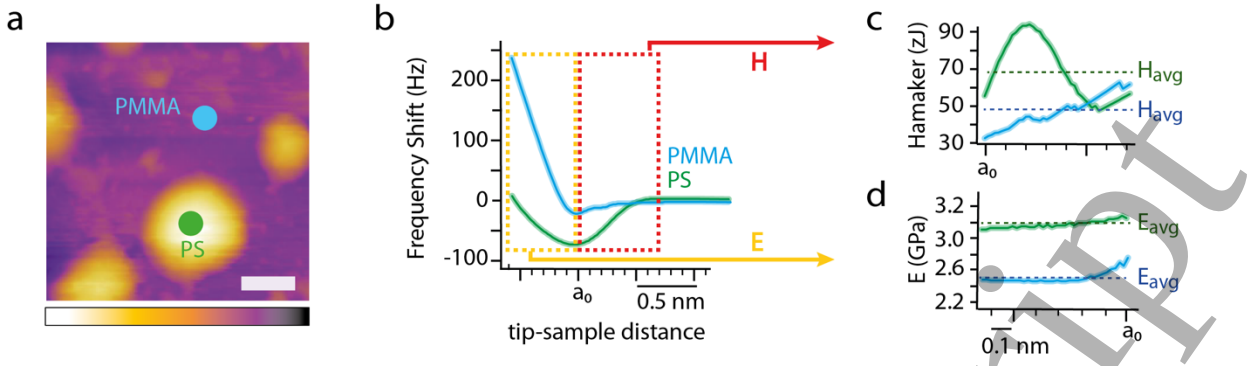

Fig. 1. Effective Hamaker constant and Young's modulus derived from FM-AFM spectroscopy conducted at specific locations of a polymeric blend sample. The derivation procedure is illustrated for curves acquired over polymethylmethacrylate (PMMA) and polystyrene (PS) regions (**a**). As the tip approaches the sample surface, the oscillation frequency shifts due to tip-sample interactions (**b**). The minimum a_0 in the frequency shift marks the transition between regions dominated by attractive dispersion forces, *H*, (red rectangle in **b**) and repulsive elastic compression, *E* (yellow rectangle in **b**), respectively. Combining the associated frequency shift with the DMT model allows determination of the effective *H* (**c**) and *E* (**d**) from the relevant regions of the curve (see text for details). The average values of *H* and *E* over the relevant curve regions are shown as dashed lines in (**c-d**) and taken as the experimental values for the measured location. The colour and scale bars in the high-resolution amplitude modulation AFM image in (**a**) are 120 nm and 1 µm, respectively. Here, the measurements were conducted with silicon cantilevers coated with Ti/Ir (Asyelec.02, Oxford Instruments, London, UK); see below for the rationale behind the choice of these probes.

The values of *H* and *E* are respectively deduced from the attractive ($d > a_0$) and repulsive ($d < a_0$) regions of the FD curve (Fig. 1b-c). The first step of the method is to derive an analytical expression for *H* and *E* based on the experimental parameters in conjunction with the DMT model. This is done using the virial theorem: for a full oscillation of the AFM cantilever vibrating at its first eigenfrequency, the virial of the tip-sample system, V_{tsc}, is equivalent to the time averaged kinetic energy of the tip[60]:

$$V_{tsc} = \frac{1}{T}\int_0^{T_0} F_{tsc}(d)\, z(t) dt, \qquad (1)$$

where F_{tsc} is the conservative part of the interaction force between the cantilever tip ensemble and the surface of the sample, described by DMT force profile as[61]

$$F_{tsc} = \begin{cases} -\dfrac{HR}{6d^2} & d \geq a_0 \\ -\dfrac{HR}{6a_0^2} + \dfrac{4E\sqrt{R}}{3}(d)^{\frac{3}{2}} & d < a_0 \end{cases} \qquad (2)$$

It is worth noting that this approach implicitly models dynamic sensing by means of a static indentation method (DMT). The conservative part of the interaction force when the cantilever taps the surface is effectively a form of contact resonance method (see Fig. 1b). The hard deformation of the tip/sample convoluted systems is however not taken into consideration, with the sample assumed to be significantly softer (smaller E) than the tip. Static indentation models have been widely used when reconstructing tip-sample interactions in dynamic AFM nanomechanical spectroscopy[25,31,40,62]. The DMT model considers vdW forces and thus can effectively approximate both the attractive and repulsive regimes of nanoscale dynamic sensing[18,63]. For the case of soft polymeric samples or where the attractive regime presents a shorter range in comparison to the deformation , the JKR model may be then suggested as an option alternative to the DMT. Using the JKR, however, renders the method significantly more complex as the work of adhesion of the probe and the sample, and hence their surface free energies, should be also taken into account[18,64]. Also, using the JKR model would require the reconstruction of the tip-sample interaction forces[39,50,51]- a step the proposed method does not require as detailed below. Significantly, considering the caveats associated with modelling the indentation part of the curves and the large number of existing AFM-based approaches focusing precisely on determining the local Young's modulus[25,31,40,62], the present study places the emphasis on the non-contact region of the oscillation and the quantification of dispersive forces.

In FM-AFM, the instantaneous displacement *z(t)* of the cantilever oscillating with amplitude, *A,* is given by

$$z(t) = A\cos(\omega t + \frac{\pi}{2}) \qquad (3)$$

Thus, the interaction potential in Eq. (1) can be approximated as[37,60]

$$V_{tsc} = -A^2 k \frac{\Delta f}{f_0} \qquad (4)$$

where k is the cantilever flexural spring constant and f_0 the resonance frequency of cantilever far from the sample.

Combining Eqs (1), (2) and (4) leads to the following analytical expressions for *H* and *E*, the effective Hamaker constant and Young's modulus of the combined tip-sample system, (see Supplementary Material section 1 for a detailed derivation of the expressions):

$$H = \frac{6kA^3\Delta f}{Rf_0}\left[\left(\frac{d+A}{A}\right)^2 - 1\right]^{3/2} \qquad d \geq a_0 \qquad (5)$$

$$E = \frac{k\Delta f}{f_0\sqrt{R}}\left[\frac{\sqrt{8A^3}}{(a_0-d)^2} + \frac{1}{\sqrt{(a_0-d)}}\right] + \frac{H\sqrt{R}}{8a_0^2(a_0-d)^{3/2}} \qquad d < a_0 \qquad (6)$$

We note that while H is defined for a specific pair of interacting materials, E describes an intrinsic property of a given material. Here E comprises information from both the sample and the indenter through the well-known relationship[18,65]:

$$E = \left(\frac{1-\nu_m^2}{E_m} + \frac{1-\nu_t^2}{E_t}\right)^{-1}, \qquad (7)$$

where ν_m (ν_t) and E_m (E_t) are the Poisson's ratio and Young's modulus of the material (the indenting tip).

As shown in Fig. 1b, E is reconstructed for the FD regime when the cantilever tip is indenting into the material, thus ensuring full contact between the two. The oscillation amplitude being constant provides a key advantage for FM-AFM spectroscopy allowing directly measuring the indentation length as the cantilever moves towards the surface[31,66,67].

Practically, at least, 100 FD curves are acquired per location and subsequently averaged; then, using the average FD curve, the experimentally determined values of H and E for the location considered are taken as the average values over the attractive, and repulsive regime, respectively, and their uncertainty taken as the standard error. This averaging procedure accounts for the uncertainty related to the imposed DMT force profile and measurement noise.

One key point to highlight is that the derived Hamaker constant does not represent single atomistic interactions but rather an average over a small (typically <100) molecules or atoms. Existing theoretical and experimental methods based on an atomistic description allow investigating vdW dispersion coefficients[8] and non-additive screening[4] between single atoms, as well as molecular adsorption distances[9], but measurements typically need to be conducted with specialist equipment in ultra-high vacuum[8,9]. Here, H is reconstructed using a simple continuum, nanoscale model thus inherently assuming average properties over the surface area probed by the AFM tip apex. The use of a continuum assumption is also responsible for the variation of H with distance observed in Fig. 1c. This is mitigated by averaging over short distances and we hence refer to H as an effective Hamaker constant. Further improvements to

the model could include quantum many-body treatment for the non-additive nature of vdW interactions[15], but such a treatment goes beyond the scope of this paper. Here, the focus is instead placed on developing an approach which can be rapidly and simply implemented with commercial AFMs, and applied both in air and liquid. A further advantage of the proposed method over existing approaches is the fact that it bypasses the need for any fitting procedures[68,69] inherent to force reconstruction strategies, significantly reducing the error on the analysis. Additionally, the direct relationship between Δf, H and E makes the analysis considerably simpler and faster. Figure 1 further highlights the potential of the proposed method in investigating local differences in H and E forces over a polymer blend sample. As expected, distinct polymethylmethacrylate (PMMA) and polystyrene (PS) domains are visible. In both cases, the effective Young's modulus decreases as the tip further indents into the material due to an increase in adhesion between the cantilever and the sample, a phenomenon well documented[18]. The behaviour of H, however, shows significant differences between PMMA and PS likely due to their different hydrophilicity and the measurements being conducted in ambient conditions (T=25 °C, relative humidity, RH = 40% ± 5). PMMA and PS exhibit water contact angles of 67° [70] and 86° [71], respectively, creating a thin water film on PMMA that changes the dielectric constant of the intervening medium. H values derived over the attractive region can vary also due to the imposed DMT force profile and measurement noise. This is mitigated by taking the average value over the entire region. To validate the technique, we first used a numerical approach with computer simulations based on a fourth-order Runge-Kutta algorithm[72,73], and exploring materials with H ranging from ~10^{-21} up to 10^{-19} J and E from ~0.1 GPa to >4 GPa. The interest of this approach is the ability to test a wider range of materials properties without changing other parameters such as surface chemistry. The simulation results show the robustness of the method in quantifying H and E for all the samples (Figs S1-2 and Supplementary Material section 2).

Before conducting a similar experimental validation on different samples, it is necessary to ascertain the robustness of the method in terms of experimental parameters. Since H and E are only observable over specific regions of the FD curves, it is likely that the choice of tip oscillation amplitude will impact the measurements. This is practically important when conducting AFM measurement because the choice of amplitude affects the size of the features that can be resolved, but also the signal-to-noise of the measurement. We investigate this issue systematically on a highly orientated pyrolytic graphite (HOPG) sample immersed in pure water. The water-HOPG interface is crucial to a wide range of technological systems from van

der Waals-based interfacial self-assembly[74] and catalysis[75] to surfactants and lubrication[28], and is hence used here as a test system. The HOPG surfaces present a range of structural features from step edges to asperities[28], offering an ideal platform to test the ability of our method with different operating amplitudes. We first image the water-HOPG interface (Fig. 2a), revealing various surface features such as step edges, terraces, point-like defects and other singularities. Choosing 6 different locations with increasing local roughness (labelled as L1-6, Fig. 2a) we conduct spectroscopic measurements with a range of oscillation amplitudes and derive *H* and *E* in each case. Roughness is arguably the simplest metric to characterise the local topography of a nanoscale region or surface sites[18,28]. The reconstructed average values for *H* and *E* are presented as functions of roughness (Fig. 2b-c). At small amplitudes (0.3-0.5 nm), a clear evolution is visible with regions exhibiting smaller roughness showing, overall, smaller *H* and greater *E* (Fig. 2b-c). This trend vanishes at larger amplitudes where *H* and *E* appear to converge to average values independently of the roughness. The fact that smaller oscillations amplitudes are more sensitive to local variations in nanoscale features is expected[28,33]. The present measurements show that for measurements of *H* and *E*, this effect tend to occur when the oscillation amplitude is comparable or smaller than the size of the local features. In such cases, *H* increases due to the larger effective surface areas interacting with the measuring tip, when compared to a perfectly flat region[18]. In contrast, the apparent *E* decreases due to sample become more deformable locally at asperities and defects[18]. Using oscillation amplitudes larger than the features length scale results in averaging out any singularities and probing an effectively *homogeneous* sample surface. *H* and *E* then tend to converge to average values which are in relatively good agreement with theoretical expectations and experimental results from the literature (2-30 zJ and 18-24 GPa, respectively). This is an important results because it demonstrates that the method is capable of distinguishing the contributions of local nanoscale features, something usually neglected by existing measurement techniques and models[76–88]. Previous dynamic and contact mode AFM studies have highlighted the fact that *H* values tend to be affected by roughness and nanoscale features[89,90]. This was achieved by implementing an AFM system within a transmission electron microscope (TEM), with the measurements performed in vacuum. While highly accurate, the need for a combined AFM-TEM system significantly limits its broad applicability[89]. Here, the proposed method can be easily implemented into standard commercial AFMs for measurements at ambient conditions and on any materials.

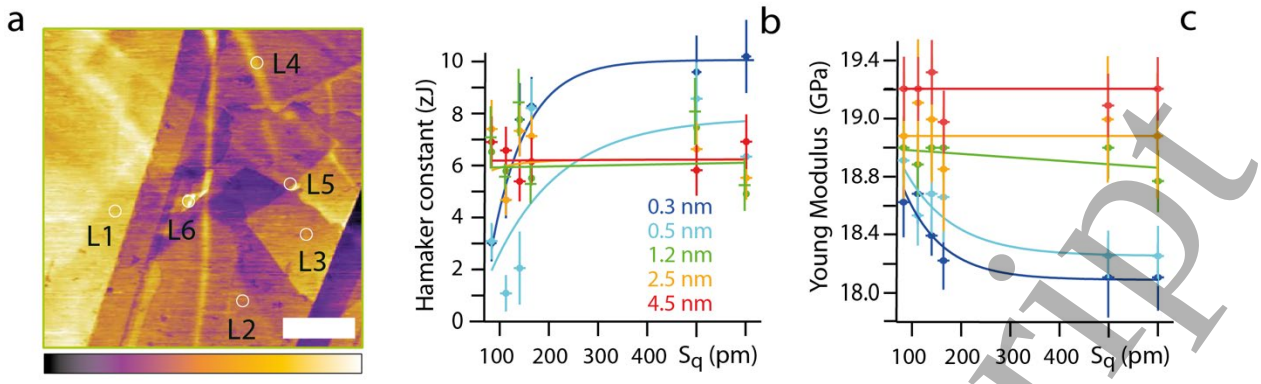

Fig. 2. Impact of nanoscale features on the effective Hamaker constant and Young's modulus at the HOPG-water interface. Imaging of the water-HOPG interface shows a wide variety of features such as step edges, terraces, point-like defects (**a**). Representative features with increasing local roughness (L1→L6) are probed using FM spectroscopy. Each location is investigated with five different oscillation amplitudes (0.3, 0.5, 1.2, 2.5 and 4.5 nm). At small oscillation amplitudes (< 1 nm), H and E vary with the sample roughness (**b-c**). This is no longer the case for larger amplitude where H and E appear roughness independent due to the local features being averaged in the measurements. The surface roughness is the root mean square value (S_q) [18] averaged over an area of ~ 50 nm^2 to account for possible experimental drift[26]. The non-linear evolution of H and E as functions of S_q has been fitted with an exponential which converges to an average value for oscillations > 0.5 nm. The colour and scale bars in the high-resolution amplitude modulation AFM image in (**a**) are 2 nm and 400 nm, respectively. Here, the measurements were performed with Arrow UHF silicon cantilevers (Nanoworld, Switzerland); see the main text for the rationale.

It is furthermore worth mentioning that the choice of oscillation amplitude has a crucial importance when using numerical methods in force reconstruction. The numerical deconvolution of the force can be ill-posed resulting in erroneous forces values, extremely sensitive to arbitrarily small errors in the oscillation amplitude. A solution to this ill-posed problem is to adjust the oscillation amplitude by means of an inflection point test[91]. The inflection point test is based on evaluating the first and third derivatives of the force at each inflection point to verify whether the curvature of the reconstructed force may change too rapidly with a consequent loss in information. Experimentally, the determination of inflection points and the calculation of the first and third derivatives are far from trivial due to the discrete nature of the data and noise with the need of data filtering based on an arbitrary choice of parameters. Experimental studies furthermore suggest that the test may yield results for the oscillation amplitude which do not maximize the signal-to-noise ratio[92]. Our proposed method

offers an analytical equation that avoids the ill-posed problem in force deconvolution, allowing for a wide range of oscillation amplitudes to be used.

Using roughness independent (>3nm) amplitudes, we then comparatively test the proposed method over 8 different samples representative of 2D materials and polymers in air at ambient conditions (see Methods section below): muscovite mica, HOPG, molybdenum disulfide (MoS_2), grown monolayers of WSe_2, $MoTe_2$ and hexagonal boron nitride (h-BN) and unmodified unstained microphase separated polystyrene-b-polymethylmethacrylate (PS-PMMA). The first three samples (HOPG, mica and MoS_2) act as a reference and the Hamaker constants describing their interaction with silicon (the AFM tip material) have previously been experimentally determined. WSe_2, $MoTe_2$ and h-BN are selected as representative 2D-materials for which, to the best of our knowledge, only theoretical predictions for H are available. Finally, a microphase separated PS-PMMA mixture is used as representative of polymeric materials. These polymers also offer a benchmark to assess the spatial accuracy of the method, allowing the selective probing of PS or PMMA domains (see Fig. 1a). The representative 2D materials are tested with commonly used silicon cantilevers[29,47,93], whereas the experiments on PS-PMMA are performed with Ti/Ir coated cantilevers. The use of different combination of AFM probes and substrates is deliberate, to validate the general applicability of the proposed method independently from a specific system or operating conditions. Additionally, the choice of tip materials used in this study is motivated by the relevance of silicon-based substrates for the growth of 2D materials, and the routine use of Ti nanofibers and Ir complexes with PS and PMMA polymers in photovoltaics[94], pH electrodes for harsh environmental conditions[95] and medical devices[96].

The Young's moduli of all the samples have been previously established with various experimental techniques[76–78,84,85,88,97,98], offering a straightforward assessment of Eq. (5). In all cases, the sample modulus E_m is derived, using Eq. (7) and assuming a tip modulus of $E_t \sim 500$ GPa for Ir[99] and $E_t \sim 150$ GPa for Si[100], and Poisson ratios of 0.26 (Ir) and 0.23 (Si)[65,100–106]. The Poisson ratios for the materials are taken from refs[65,79,107–112]. The results are shown in Fig. 3 for all the materials studied.

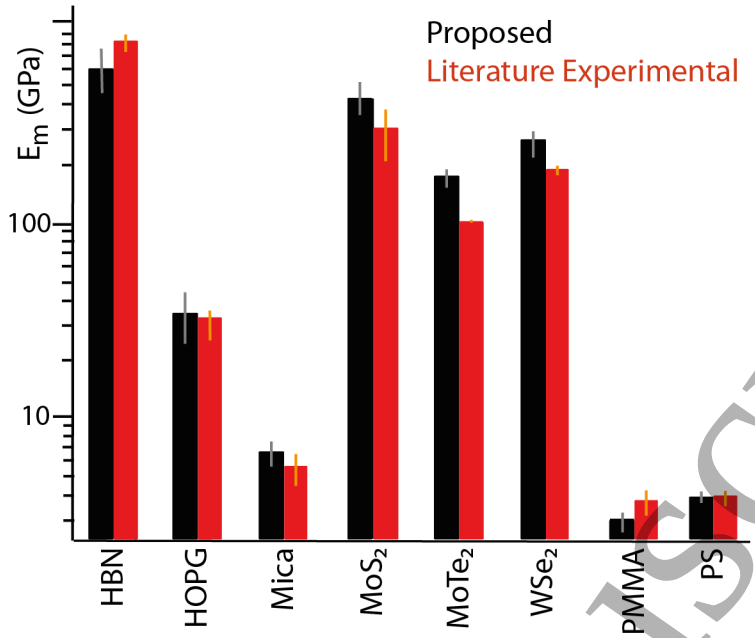

Fig. 3. Comparison of the E_m values derived in this study using a combination of FM-AFM spectroscopy and Eqs. (5) and (7) (black) with published values from other experimental studies (red). The measured and literature value agree within error for all the materials except for $MoTe_2$ and WSe_2 where the values differ by ~ 30 % within error. The literature values are from the following refs: HBN[77], HOPG[76,78], mica[97], MoS_2[84,113,114], $MoTe_2$[84,98], WSe_2[85,88], PMMA[86] and PS[86]. Note the log scale to aid comparison across the wide range of values.

Comparison between the derived and literature values indicate an excellent agreement within error, except for $MoTe_2$ and WSe_2 where larger differences are visible. Even for these materials, the differences between measured and literature values are ~ 30 % within error, a remarkable feat considering the broad range of moduli being probed. The specific experimental conditions and sample preparation are also likely to influence the values measured with no means of ensuring identical conditions between the present and literature values. The good agreement of our measured values with the literature for the PS-PMMA polymeric blend rules out tip convolutions effects[28,115]: after selecting the region of interest (Fig. 1), our approach accurately investigates its nanomechanical properties without any evident tip geometry dependent artifacts or bias due to the cantilever inclination with respect to the sample surface[115]. Further studies are however needed to validate the impact of probe geometry on the proposed method and to further implement it also using available models for AFM tips/surface interactions accounting for tip geometry[2,66,116]. Additionally, although the Young moduli derived for the stiffer material appear in good agreement with the literature, the measurement

is ambiguous since the tip itself has comparable stiffness. A more sophisticated model considering the tip deformation may be needed in some cases.

Overall, Fig. 3 validates the approach developed in this study to determine *E*, a well-characterized quantity. Determining *H* is more challenging with limited experimental benchmarking available. For five out of the eight materials investigated here, only theoretical predictions are available, based on the Lifshitz theory[117–119]. The theoretical calculations assume that the tip, the sample and the medium in-between are all perfectly homogeneous. This is obviously a simplification, especially for the in-between medium where condensation water molecules and adsorbed contaminants can affect the dielectric constant[120]. We therefore first validate the proposed method with the three systems for which experimental *H* values are available: HOPG, mica, and MoS_2, each interacting with commercial silicon or silicon nitride tips[47,121]. Silicon tips are well-known to form a surface oxide layer when exposed to ambient conditions, something common for all commercial tips. It is therefore reasonable to assume the silicon tips to behave as silicon nitride since the latter exhibits properties in-between pure silicon and silicon oxide (see Supplementary Material section 3 for the relevant data). Our experiments being conducted in ambient conditions, water molecules tend to adsorb at the surface of the sample and the tip forming complete ordered layers at hydrophilic interfaces. On mica, ambient humidity creates ice-like structure due to epitaxial effects with the substrate lattice constant approximately matching that of the hexagonal ice basal plane[33]. To some extent, ice-like layer can also be assumed to form at the interface with HOPG and MoS_2 which lie at the boundary between hydrophilic and hydrophobic (see Supplementary Material section 4). In principle, adsorption of airborne hydrocarbons can also affect the measurements and is well known to increase hydrophobicity over time[122], but the present measurements were conducted on freshly cleaved surfaces. In all cases, the tip is bound to have an absorbed water layer on its surface and we hence always derived theoretical prediction assuming an ice-like water layer between the tip and the different substrates[29] (see Supplementary Material section 3 for the details on the theoretical calculations). Fig. 4 shows, for the three materials, the comparison of measured *H* vs the experimental data obtained from the literature and theoretical predictions. For each material the measured, literature and theoretical data agree within error, with a particularly good agreement between the measured and the literature values. In the case of mica, the literature values were adjusted to match our experimental humidity (40% ± 5%) by interpolating the values reported for a dry[117,121] and humidity saturated environment[117]. In the case of MoS_2, the theoretical prediction appears way off, despite agreeing with the

experimental values when the large error is considered. Relaxing the assumption of a water layer would only increase the predicted *H* value, suggesting a fundamental problem with the prediction. Part of the issue comes from the difficulty in obtaining a relevant refractive index for MoS_2, a key parameter in the prediction. Depending on the publications and the range of wavelengths considered[123–125], reported refractive index values can vary by more than 100% rendering objective predictions challenging.

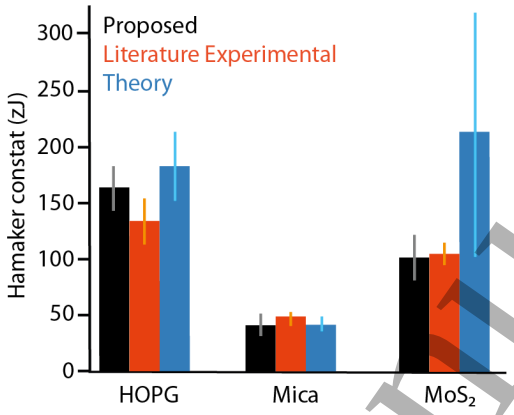

Fig. 4. Comparison of *H* constants measured in this study (black) with experimental values from the literature (red)[47,121] and theoretical predictions (blue). The literature experimental values are from ref.[121] for mica, and ref.[47] for HOPG and MoS_2. In all cases, the *H* values represent the interactions between the stated material and the silicon AFM tip in air at ambient conditions; the different intervening medium in comparison to the measurements shown in Fig. 2 (water) accounts for the different values of *H* for HOPG. For mica, the literature value was obtained by linear interpolation of the reported dry and water-saturated values to match our 40% experimental humidity. The theoretical predictions assume a homogeneous ice-like layer of adsorbed water molecules on the surface, and the silicon cantilever undergoing an effective surface oxidation (see Supplementary Material section 3). Measurements over mica could not be achieved in water, presumably due to its strong hydrophilicity[18,29,33]. The error bars on the theoretical predictions represent the range of refractive indices and dielectric constants reported in the literature (see Supplementary Material section 3)

Aside from the difficulty with the theoretical prediction for MoS_2, the excellent agreement between the measured, reported and theoretical *H* values validates the proposed method. We therefore derived the first experimental *H* constants for the other five materials with only theoretical calculations as a point of comparison. All the materials probed are weakly hydrophilic (see Supplementary Material section 4) and an epitaxial water layer is expected

(also assumed in the calculations). This is a common feature for some of the most wide spread 2D materials based on graphene and transition metal dichalcogenides[126], as well as for a wide range of technologically relevant polymers with applications, for example, in drug delivery[127], wastewater treatment[128] and thermally insulating foams[129]. The calculations were therefore conducted under the same assumptions as before. The results, presented in Fig. 5, show an excellent agreement between our measurements and the theoretical predictions within error.

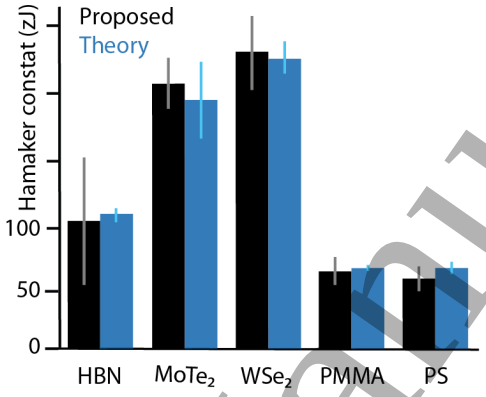

Fig. 5. Comparison of the values for *H* derived experimentally with the proposed method and calculated from theory. As for the previous materials, the theoretical calculations assume an adsorbed layer of water molecules on the surfaces (ambient conditions) thereby affecting the dielectric response of the intervening medium[130,131] (see also Supplementary Material section 2).

Taken together our experimental results validate the proposed experimental method and show that it is possible to derive simultaneously *H* and *E* with high spatial accuracy and without damaging either the probe or the sample.

It is worth mentioning that the proposed method approximates the probe surface interacting with the substrate as the tip apex. While our simplified modelling is among the most popular approaches in the AFM community[18,31,46,60,132,133], it may be argued that, vdW attractions being relatively long-ranged, the tip shank contribution should be considered. Models have been hence developed in this sense[68,134]. These approaches are however highly sensitive to the choice of fitting parameters[134]. Furthermore, in the case of the range for vdW attractive forces being smaller than tip radius, they may overestimate the Hamaker constant. This may explain why, incorporating the tip shank contribution in our model, the results differ from the theoretical or

literature values (Fig. S3 in the Supplementary Material section 5). It should be also noted that this additional contribution is only approximated (see Eq. S18 in Supplementary Material section 5) and has not been analytically resolved within our proposed method.

It is also worth discussing some limitations and possible sources of error in conducting the measurements. First, as obvious from the previous discussion, environmental factors such as humidity and airborne contamination of the material and the tip can dramatically influence the value derived for *H*. The issue is not specific to the proposed method but common to all experimental measurements of dispersion forces. Measurements should therefore be conducted in an environment which best replicates that of the desired application, and with a suitable degree of care. Second, the methodology itself relies on the accurate determination of the probe's stiffness[135,136], its effective tip radius of curvature[137], the pull-off deflection force and the cut-off distance[121]. These parameters being fundamental when reconstructing physical quantities from standard AFM spectroscopy measurements, there exist, however, well established protocols[2,37,138] to precisely and accurately determine them minimising the associated uncertainty. It is therefore possible to accurately and reliably quantify the error on *H* and *E* resulting from measurements with the proposed method.

Conclusions

In this study, we present a fully analytical method to derive the Hamaker constant and Young's modulus of a sample material from experimental observables acquired in AFM spectroscopic measurements. The derived Hamaker constant and Young's modulus represent an average over a small (typically <100) molecules or atoms. The method offers a spatial resolution comparable to the size of the AFM tip (typically <10 nm) and can be easily implemented on most commercial AFMs. We validate our approach on a range of materials, from relatively stiff 2D materials to compliant polymers films, paving the way for its adoption in the nanoscale design of 2D materials and polymer-based devices. It could, for example, help disentangle the effect of doping on functional coatings[139,140] and energy storage materials[141]. The ease of use and the high spatial resolution would be also help provide new insights into the role of vdW forces in the function and assembly of 2D heterostructures on different substrates[6,142].

Methods

Materials. Experiments are conducted using a commercial Cypher ES AFM (Oxford Instruments, CA, USA) equipped with temperature control. We use two types of commercial cantilevers with their flexural calibration being performed using their thermal spectrum[143]:

1. Arrow UHF silicon cantilevers (Nanoworld, Switzerland). Arrow cantilevers were found to have a stiffness k_f in the range 1.6–5.0 N m^{-1}, a Q-factor of 360 ± 10 and a flexural resonance frequency of 2040 ± 50 kHz. The mechanical properties of the cantilevers are consistent with the literature[29,144].

2. Asyelec.02 silicon cantilevers coated with Ti/Ir (5/20) (Oxford Instruments, London, UK). The probes are found to have flexural stiffness, k, of 46.0 ± 0.3 nN/nm, a Q-factor of 630.0 ± 0.3 and a resonance frequency of 318 ± 1 kHz. In comparison to standard silicon tips[29,145], the stiffness and the Ir-coating of tips ensures increased sensitivity through higher Q-factor[37] and high wear resistance[146], respectively.

High-quality V1 muscovite mica discs, HOPG and MoS_2 were purchased from SPI supplies, West Chester, PA, USA; grown monolayers of WSe_2, $MoTe_2$ and h-BN, each of them transferred to a SiO_2/Si substrate, were custom made by 2D Semiconductors, NY, USA; unmodified unstained microphase separated PS-PMMA was purchased from Nanosurf AG, Liestal, Switzerland. Thorough cleaning procedures were implemented as detailed in the Supplementary Material section 6.

Imaging. All the experiments are performed in air at 25 °C, unless otherwise specified (*e.g.* HOPG fully immersed in water, Fig. 2). All the experiments were performed ensuring that at the time of the measurements the ambient RH was within the range 40% ± 5%, thus minimizing any variations in the potential capillary forces experienced by the probe. The RH was monitored with a thermo-hygrometer (Fluka Corporation, Washington, USA). Thermal equilibrium is achieved ensuring that the cooling/heating rate of the temperature control system within the AFM is constant for, at least, 20 minutes[29,138]. The sample surfaces are imaged both before and after performing force spectroscopy. This allows selecting, with sub-nanometer precision, the locations to probe by force spectroscopy, as well as ensuring the absence of any significant drift after conducting the spectroscopy. Furthermore, this also helps rule out the presence of any adsorbed contaminants directly visible when imaging. High-resolution imaging is performed in amplitude modulation AFM (AM-AFM). In this mode, the cantilever

is oscillated at a frequency close to resonance. Away from the material surface, the cantilever oscillates with a free amplitude A_0. As the tip approaches the sample, the oscillation amplitude is reduced due to the interactions with the sample surface. The material surface is raster-scanned keeping a set point amplitude, A_s, constant by means of a feedback loop. The ratio A_s/A_0 is set as high as possible so as to ensure gentle imaging. The sample topography is reconstructed using the amplitude corrections. The phase lag between the cantilever oscillation and the driving oscillation can vary freely and provides information on the tip-sample interactions[28,29,147].

Force spectroscopy is performed in frequency modulation. The cantilever approaching the sample surface, its oscillation amplitude and frequency are kept constant using two feedback loops. For the measurements exploring the role of oscillation amplitude presented in Fig. 2, the HOPG-water is investigated using an Arrow UHF cantilever with 5 different amplitudes (0.3, 0.5, 1.2, 2.5, 4.5 nm). The set amplitude is 3.00 nm for the 2D-materials and 8.00 nm for the PS-PMMA (Fig. 3-5). Frequency and amplitude corrections are acquired as a function of the tip-sample distance[37] over >3 (typically 5) different locations for each substrate resulting in >100 force-distance curves that are subsequently averaged. Each set of experiment, including both imaging and spectroscopy, is repeated at least three times to ensure reproducibility.

Data availability

The authors declare that the data supporting the findings of this study are available within the paper and its supplementary information files. Data are also available from the corresponding author upon reasonable request.

Competing Interests

The Authors declare no Competing Financial or Non-Financial Interests.

Author Contributions

A. F. P. conceived the idea and developed the mathematical model. C.C. planned and conducted the experiments. C. C. and A. F. P. analysed the data. All the others contributed to writing the paper.

C.C. is grateful to the Institute of Advanced Studies, Durham University and to the Physics Department, Durham University (Developing Talent Scheme) for the financial support.

References

1. Novoselov, K. S., Mishchenko, A., Carvalho, A. & Castro Neto, A. H. 2D materials and van der Waals heterostructures. *Science,* **353**, aac9439 (2016).
2. Garcia, R. Nanomechanical mapping of soft materials with the atomic force microscope: Methods, theory and applications. *Chem. Soc. Rev.* **49**, 5850–5884 (2020).
3. Labardi, M. & Capaccioli, S. Tuning-fork-based piezoresponse force microscopy. *Nanotechnol.* **32**, 445701 (2021).
4. Tsoi, S., Dev, P., Friedman, A. L., Stine, R., Robinson, J. T., Reinecke, T. L., & Sheehan, P. E. Van der Waals screening by single-layer graphene and molybdenum disulfide. *ACS Nano* **8**, 12410–12417 (2014).
5. Gobre, V. V., & Tkatchenko, A. Scaling laws for van der Waals interactions in nanostructured materials. *Nat. Commun.* **4**, 2341 (2013).
6. Li, Z., Lv, Y., Ren, L., Li, J., Kong, L., Zeng, Y., Tao, Q., Wu, R., Ma, H., Zhao, B., Wang, D., Dang, W., Chen, K., Liao, L., Duan, X., Duan X., & Liu, Y. Efficient strain modulation of 2D materials via polymer encapsulation. *Nat. Commun.* **11**, 1151 (2020).
7. Rokni, H. & Lu, W. Direct measurements of interfacial adhesion in 2D materials and van der Waals heterostructures in ambient air. *Nat. Commun.* **11**, 5607 (2020).
8. Wagner, C., Fournier, N., Ruiz, V. G., Li, C., Müllen, K., Rohlfing, M., Tkatchenko, A.,Temirov, R. & Tautz, F. S. Non-additivity of molecule-surface van der Waals potentials from force measurements. *Nat. Commun.* **5**, 5568 (2014).
9. Schuler, B., Liu, W., Tkatchenko, A., Moll, N., Meyer, G., Mistry, A., Fox, D. & Gross, L. Adsorption geometry determination of single molecules by atomic force microscopy. *Phys. Rev. Lett.* **111**, 106103 (2013).
10. Wang, Y., He, Q., Ming, W., Du, M.H., Lu, N., Cafolla, C., Fujioka, J., Zhang, Q., Zhang, D., Shen, S., Lyu, Y., N'Diaye, A.T., Arenholz, E., Gu, L., Nan, C., Tokura, Y., Okamoto, S. & Yu, P. Robust ferromagnetism in highly strained $SrCoO_3$ thin films. *Phys. Rev. X* **10**, 021030 (2020).
11. Li, W., Zhu, B., Zhu, R., Wang, Q., Lu, P., Sun, Y., Cafolla, C., Qi, Z., Chen, A., Gao, P., Wang, H., He, Q., Zhang, K.H.L., MacManus-Driscoll, J.L. Atomic-scale control of electronic structure and ferromagnetic insulating state in perovskite oxide superlattices by long-range tuning of BO6 octahedra. *Adv. Funct. Mater.* **30**, 2001984 (2020).
12. Glavin, N.R., Rao, R., Varshney, V., Bianco, E. Apte, A., Roy, A., Ringe, E., Ajayanet, P.M. Emerging applications of elemental 2D materials. *Adv. Mater*. **32**, 1904302 (2020).

13. Zhang, S., Ma, T., Erdemir, A. & Li, Q. Tribology of two-dimensional materials: from mechanisms to modulating strategies. *Mater. Today* **26**, 67-86 (2019).
14. Ambrosetti, A., Ferri, N., DiStasio, R. A. & Tkatchenko, A. Wavelike charge density fluctuations and van der Waals interactions at the nanoscale. *Science* **351**, 1171–1176 (2016).
15. Hauseux, P., Nguyen, T. T., Ambrosetti, A., Ruiz, K. S., Bordas, S. P., & Tkatchenko, A. From quantum to continuum mechanics in the delamination of atomically-thin layers from substrates. *Nat. Commun.* **11**, 1651 (2020).
16. Tripathi, M., Lee, F. Michail, A., Anestopoulos, D., McHugh, J.G., Ogilvie, S.P., Large, M.J., Graf, A. A., Lynch, P.J., Parthenios, J., Papagelis, K., Roy, S., Saadi, M. A. S. R., Rahman, M.M. Pugno, N.M., King, A.A.K., Ajayan, P.M. & Dalto, A.B.. Structural defects modulate electronic and nanomechanical properties of 2D materials. *ACS Nano* **15**, 2520-2531 (2021).
17. Guo, H. W., Hu, Z., Liu, Z. B. & Tian, J. G. Stacking of 2D materials. *Adv. Funct. Mater.* **31**, 2007810 (2021).
18. Mate, C.M. & Carpick, R.W. *Tribology on the small scale: a modern textbook on friction, lubrication, and wear*. (Oxford University Press, New York, 2019).
19. Vashisth, A., Khatri, S., Hahn, S.H., Zhang, W., van Duin, A.C.T., & Naraghi, M. Mechanical size effects of amorphous polymer-derived ceramics at the nanoscale: experiments and ReaxFF simulations. *Nanoscale* **11**, 7447-7456 (2019).
20. Li, Q., Barrett, D. G., Messersmith, P. B. & Holten-Andersen, N. Controlling hydrogel mechanics via bio-inspired polymer-nanoparticle bond dynamics. *ACS Nano* **10**, 1317-1324 (2016).
21. Vanroy, B., Wü, M. & Napolitano, S. Remotely controlling the crystallization of thin polymer coatings. *Macromolecules* **53**, 4882-4888 (2020).
22. Kadri, K., Peixinho, J., Salez, T., Miquelard-Garnier, G., & Sollogoub, C. Dewetting of a thin polymer film under shear. *Polymer* **235**, 124283 (2021).
23. Schulman, D. S., Arnold, A. J., & Das, S. Contact engineering for 2D materials and devices. *Chem. Soc. Rev.* **47**, 3037-3058 (2018).
24. Oliver, W. C. & Pharr, G. M. Measurement of hardness and elastic modulus by instrumented indentation: advances in understanding and refinements to methodology. *J. Mater. Res.* **19**, 3–20 (2004).
25. Liu, Y., Sokolov, I., Dokukin, M. E., Xiong, Y. & An Peng, P. Can AFM be used to measure absolute values of Young's modulus of nanocomposite materials down to the

nanoscale? *Nanoscale* **12**, 12432-12443 (2020).

26. Rejhon, M., Lavini, F., Khosravi, A., Shestopalov, M., Kunc, J., Tosatti, E., & Riedo, E. Relation between interfacial shear and friction force in 2D materials. *Nat. Nanotechnol.* **17**, 1280-1287 (2022).
27. Cellini, F., Gao, Y. & Riedo, E. *Å*-Indentation for non-destructive elastic moduli measurements of supported ultra-hard ultra-thin films and nanostructures. *Sci. Rep.* **9**, 4075 (2019).
28. Cafolla, C., Foster, W. & Voïtchovsky, K. Lubricated friction around nanodefects. *Sci. Adv.* **6**, eaaz3673 (2020).
29. Cafolla, C. & Voïtchovsky, K. Impact of water on the lubricating properties of hexadecane at the nanoscale. *Nanoscale* **12**, 14504-14513 (2020).
30. Mangolini, F., McClimon, J. B., Rose, F. & Carpick, R. W. Accounting for nanometer-thick adventitious carbon contamination in X-ray absorption spectra of carbon-based materials. *Anal. Chem.* **86**, 12258-12265 (2014).
31. Payam, A. F., Morelli, A. & Lemoine, P. Multiparametric analytical quantification of materials at nanoscale in tapping force microscopy. *Appl. Surf. Sci.* **536**, 147698 (2021).
32. Melcher, J., Martínez-Martín, D., Jaafar, M., Gómez-Herrero, J. & Raman, A. High-resolution dynamic atomic force microscopy in liquids with different feedback architectures. *Beilstein J. Nanotechnol.* **4**, 153-163 (2013).
33. Cafolla, C. & Voïtchovsky, K. Lubricating properties of single metal ions at interfaces. *Nanoscale* **10**, 11831-11840 (2018).
34. Ricci, M., Trewby, W., Cafolla, C. & Voïtchovsky, K. Direct observation of the dynamics of single metal ions at the interface with solids in aqueous solutions. *Sci. Rep.* **7**, 43234 (2017).
35. Ricci, M., Spijker, P. & Voïtchovsky, K. Water-induced correlation between single ions imaged at the solid-liquid interface. *Nat. Commun.* **5**, 4400 (2014).
36. Miller, E.J., Trewby, J., Payam, A.F., Piantanida, L., Cafolla, C, & Voitchovsky, K. Sub-nanometer resolution imaging with amplitude-modulation atomic force microscopy in liquid. *J. Vis. Exp.* e54924 (2016).
37. García, R. & Pérez, R. Dynamic atomic force microscopy methods. *Surf. Sci. Rep.* **47**, 197-301 (2002).
38. Payam, A. F., Ramos, J. R. & Garcia, R. Molecular and nanoscale compositional contrast of soft matter in liquid: Interplay between elastic and dissipative interactions. *ACS Nano* **6**, 4663-4670 (2012).

39. Sader, J. E., Uchihashi, T., Higgins, M.J., Farrell, A., Nakayama, Y., & Jarvis, P. Quantitative force measurements using frequency modulation atomic force microscopy-theoretical foundations. *Nanotechnol.* **16**, S94 (2005).
40. Herruzo, E. T., Perrino, A. P. & Garcia, Fast nanomechanical spectroscopy of soft matter. *Nat. Commun.* **5**, 3126 (2014).
41. Labuda, A., Kocun, M., Meinhold, W., Walters, D. & Proksch, R. Generalized Hertz model for bimodal nanomechanical mapping. *Beilstein J. Nanotechnol.* **7**, 970–982 (2016).
42. Horn, R. G., Clarke, D. R. & Clarkson, M. T. Direct measurement of surface forces between sapphire crystals in aqueous solutions. *J. Mater. Res.* **3**, 413–416 (1988).
43. Médout-Marère, V. A simple experimental way of measuring the Hamaker constant A_{11} of divided solids by immersion calorimetry in apolar liquids. *J. Colloid Interface Sci.* **228**, 434-437 (2000).
44. Zhang, Y., Tian, R., Yang, S., Guo, X. & Li, H. Toward an approach for determining the Hamaker constant of soft materials using dynamic light scattering. *Colloids Surf, A Physicochem Eng Asp* **630**, 127604 (2021).
45. Shahidzadeh, N., Bonn, D., Ragil, K., Broseta, D. & Meunier, J. Sequence of two wetting transitions induced by tuning the hamaker constant. *Phys. Rev. Lett.* **80**, 3992–3995 (1998).
46. Das, S., Sreeram, P. A. & Raychaudhuri, A. K. A method to quantitatively evaluate the Hamaker constant using the jump-into-contact effect in atomic force microscopy. *Nanotechnol.* **18**, 035501 (2007).
47. Krajina, B. A., Kocherlakota, L. S. & Overney, R. M. Direct determination of the local Hamaker constant of inorganic surfaces based on scanning force microscopy. *J. Chem. Phys.* **141**, 164707 (2014).
48. Polesel-Maris, J., Guo, H., Zambelli, T., & Gauthier, S. Mapping van der Waals forces with frequency modulation dynamic force microscopy. *Nanotechnol.* **17**, 4204 (2006).
49. Payam, A. F., Martin-Jimenez, D. & Garcia, R. Force reconstruction from tapping mode force microscopy experiments. *Nanotechnol.* **26**, 185706 (2015).
50. Sader, J. E. & Jarvis, S. P. Accurate formulas for interaction force and energy in frequency modulation force spectroscopy. *Appl. Phys. Lett.* **84**, 1801-1803 (2004).
51. Kim, S., Ko, J.-H. & Jhe, W. Universal theory of dynamic force microscopy for exact and robust force reconstruction using multiharmonic signal analysis. *Phys. Rev. Lett.* **126**, 076804 (2021).

52. Gotsmann, B., Anczykowski, B., Seidel, C. & Fuchs, H. Determination of tip-sample interaction forces from measured dynamic force spectroscopy curves. *Appl. Surf. Sci.* **140**, 314-319 (1999).

53. Giessibl, F. J. A direct method to calculate tip-sample forces from frequency shifts in frequency-modulation atomic force microscopy. *Appl. Phys. Lett.* **78**, 123–125 (2001).

54. Lee, M. & Jhe, W. General theory of amplitude-modulation atomic force microscopy. *Phys. Rev. Lett***. 97**, 036104 (2006).

55. Hu, S. & Raman, A. Inverting amplitude and phase to reconstruct tip-sample interaction forces in tapping mode atomic force microscopy. *Nanotechnol.* **19**, 375704 (2008).

56. O'Shea, S. J., Gosvami, N. N., Lim, L. T. W. & Hofbauer, W. Liquid atomic force microscopy: solvation forces, molecular order, and squeeze-out. *Jpn. J. Appl. Phys.* **49**, 08LA01 (2010).

57. Ludwig, M. & von Klitzing, R. Recent progress in measurements of oscillatory forces and liquid properties under confinement. *Curr. Opin. Colloid Interface Sci.* **47**, 137-152 (2020).

58. Butt, H. J., Cappella, B. & Kappl, M. Force measurements with the atomic force microscope: Technique, interpretation and applications. *Surf. Sci. Rep.* **59**, 1–152 (2005).

59. Payam, A. F. Modelling and nanoscale force spectroscopy of frequency modulation atomic force microscopy. *Appl. Math. Model.* **79**, 544-554 (2020).

60. Dagdeviren, O. E., Zhou, C., Altman, E. I. & Schwarz, U. D. Quantifying tip-sample interactions in vacuum using cantilever-based sensors: an analysis. *Phys. Rev. Applied* **9**, 044040 (2018).

61. Hölscher, H. & Schwarz, U. D. Theory of amplitude modulation atomic force microscopy with and without Q-Control. *Int. J. Non. Linear. Mech.* **42**, 608-625 (2007).

62. Dokukin, M. E. & Sokolov, I. Quantitative mapping of the elastic modulus of soft materials with HarmoniX and PeakForce QNM AFM modes. *Langmuir* **28**, 16060–16071 (2012).

63. Raman, A., Melcher, J. & Tung, R. Cantilever dynamics in atomic force microscopy. *Nano Today* **3**, 20–27 (2008).

64. Lin, D. C. & Horkay, F. Nanomechanics of polymer gels and biological tissues: a critical review of analytical approaches in the Hertzian regime and beyond. *Soft Matter* **4**, 669–682 (2008).

65. Abooalizadeh, Z., Sudak, L. J. & Egberts, P. Nanoscale spatial mapping of mechanical

properties through dynamic atomic force microscopy. *Beilstein J. Nanotechnol.* **10**, 1332 (2019).

66. Benaglia, S., Amo, C. A. & Garcia, R. Fast, quantitative and high resolution mapping of viscoelastic properties with bimodal AFM. *Nanoscale* **11**, 15289–15297 (2019).
67. Lai, C. Y., Santos, S. & Chiesa, M. Systematic multidimensional quantification of nanoscale systems from bimodal atomic force microscopy data. *ACS Nano* **10**, 6265–6272 (2016).
68. Ebeling, D., van den Ende, D. & Mugele, F. Electrostatic interaction forces in aqueous salt solutions of variable concentration and valency. *Nanotechnol.* **22**, 305706 (2011).
69. Dishon, M., Zohar, O. & Sivan, U. From repulsion to attraction and back to repulsion: The effect of NaCl, KCl, and CsCl on the force between silica surfaces in aqueous solution. *Langmuir* **25**, 2831–2836 (2009).
70. Tokuda, K., Ogino, T., Kotera, M. & Nishino, T. Simple method for lowering poly(methyl methacrylate) surface energy with fluorination. *Polym. J.* **47**, 66–70 (2015).
71. Li, Y., Pham, J. Q., Johnston, K. P. & Green, P. F. Contact Angle of Water on Polystyrene Thin Films: Effects of CO 2 Environment and Film Thickness. *Langmuir* 23, 9785-9793 (2007).
72. Worou, C. N., Kang, J., Shen, J., Yan, P., Wang, W., Gong, Y., & Chen, Z. Runge–kutta numerical method followed by Richardson's extrapolation for efficient ion rejection reassessment of a novel defect-free synthesized nanofiltration membrane. *Membranes* **11**, 130 (2021).
73. Gauthier, M., Pérez, R., Arai, T., Tomitori, M. & Tsukada, M. Interplay between nonlinearity, scan speed, damping, and electronics in frequency modulation atomic-force microscopy. *Phys. Rev. Lett*. **89**, 146104 (2002).
74. Voïtchovsky, K., Giofrè, D., José Segura, J., Stellacci, F. & Ceriotti, M. Thermally-nucleated self-assembly of water and alcohol into stable structures at hydrophobic interfaces. *Nat. Commun.* **7**, 13064 (2016).
75. Foster, W., Aguilar, J. A., Kusumaatmaja, H., & Voïtchovsky, K. *In situ* molecular-level observation of methanol vatalysis at the water–graphite interface. *ACS appl Mater. Interfaces* **10**, 34265-34271 (2018).
76. Eskelsen, J.R., Qi, Y., Schneider-Pollack, S., Schmitt, S., Hipps, K. W., & Mazur, U. Correlating elastic properties and molecular organization of an ionic organic nanostructure. *Nanoscale* **6,** 316-327 (2014).

77. Wang, W., Li, Z., Marsden, A. J., Bissett, M. A. & Young, R. J. Interlayer and interfacial stress transfer in hBN nanosheets. *2D Mater.* **8**, 035058 (2021).

78. Castellanos-Gomez, A., Poot, M., Amor-Amorós, A., Steele, G. A., van der Zant, H. S., Agraït, N., & Rubio-Bollinger, G.Mechanical properties of freely suspended atomically thin dielectric layers of mica. *Nano Res.* **5**, 550–557 (2012).

79. Bertolazzi, S., Brivio, J. & Kis, A. Stretching and breaking of ultrathin MoS 2. *ACS Nano* **5**, 9703–9709 (2011).

80. Sun, Y., Pan, J., Zhang, Z., Zhang, K., Liang, J., Wang, W., Yuan, Z., Hao, Y., Wang, B., Wang, J., Wu, Y., Zheng, J., Jiao, L., Zhou, S., Liu, K., Cheng, C., Duan, W., Xu, Y., Yan, Q. & Liu, K. Elastic properties and fracture behaviors of biaxially deformed, polymorphic $MoTe_2$. *Nano Lett.* **19**, 761-769 (2019).

81. Pereira Júnior, M.L., Viana de Araújo, C. M., De Sousa, J. M., de Sousa Júnior, R. T., Roncaratti Júnior, L. F., Ferreira Giozza, W., & Ribeiro Júnior, L. A. On the elastic properties and fracture patterns of MoX_2 (X = S, Se, Te) membranes: a reactive molecular dynamics study. *Condens. Matter* **5**, 73 (2020).

82. Zhan, H., Tan, X., Xie, G. & Guo, D. Reduced fracture strength of 2D materials induced by interlayer friction. *Small* **17**, 2005996 (2021).

83. Young's Modulus, tensile strength and yield strength values for some materials https://www.engineeringtoolbox.com/young-modulus-d_417.html. (Accessed: 30th July 2023)

84. Chang, J., Toga, K. B., Paulsen, J. D., Menon, N. & Russell, T. P. Thickness dependence of the Young's modulus of polymer thin films. *Macromolecules* **51**, 6764-6770 (2018).

85. Zhang, R., Koutsos, V. & Cheung, R. Elastic properties of suspended multilayer WSe2. *Appl. Phys. Lett.* **108**, 042104 (2016).

86. Xiao, J., Zhang, L., Zhou, K., Li, J., Xie, X., & Li, Z. Anisotropic friction behaviour of highly oriented pyrolytic graphite. *Carbon* **65**, 53-62 (2013).

87. Falin, A., Holwill, M., Lv, H., Gan, W., Cheng, J., Zhang, R., Qian, D., Barnett, M.R., Santos, E.J.G., Novoselov, K.S., Tao, T., Wu, X. & Li, L. H. Mechanical properties of atomically thin tungsten dichalcogenides: WS_2 , WSe_2, and WTe_2. *ACS Nano* **15**, 50 (2021).

88. Choi, W. R., Hong, J. H., You, Y. G., Campbell, E. E. B. & Jhang, S. H. Suspended $MoTe_2$ field effect transistors with ionic liquid gate. *Appl. Phys. Lett.* **119**, 223105 (2021).

89. Chan, N., Lin, C., Jacobs, T., Carpick, R. W. & Egberts, P. Quantitative determination of the interaction potential between two surfaces using frequency-modulated atomic force microscopy. *Beilstein J. Nanotechnol.* **11**, 729–739 (2020).

90. Jacobs, T. D. B., Lefever, J. A. & Carpick, R. W. Measurement of the Length and Strength of Adhesive Interactions in a Nanoscale Silicon-Diamond Interface. *Adv. Mater. Interfaces* **2**, 1400547 (2015).

91. Sader, J. E., Hughes, B. D., Huber, F. & Giessibl, F. J. Interatomic force laws that evade dynamic measurement. *Nat. Nanotechnol.* **13**, 1088-1091 (2018)

92. Huber, F. & Giessibl, F. J. Experimental use of the inflection point test for force deconvolution in frequency-modulation atomic force microscopy to turn an ill-posed situation into a well-posed one by proper choice of amplitude. *J. Appl. Phys.* **127**, (2020).

93. Cafolla, C. & Voïtchovsky, K. Real-time tracking of ionic nano-domains under shear flow. *Sci. Rep.* **11**, 19540 (2021).

94. Howarth, A. J., Davies, D. L., Lelj, F., Wolf, M. O. & Patrick, B. O. Tuning the emission lifetime in bis-cyclometalated iridium(III) complexes bearing iminopyrene ligands. *Inorg. Chem.* **53**, 11882–11889 (2014).

95. Park, J., Kim, M. & Kim, S. Surface renewable nano-iridium oxide polymeric composite pH electrodes. *Sens. Actuators B Chem.* **204**, 197-202 (2014).

96. Gad, M. M. & Abualsaud, R. Behavior of PMMA denture base materials containing titanium dioxide nanoparticles: a literature review. *Int. J. Biomater.* **2019**, 190610 (2019).

97. Jin, D.W., Ko, Y. J., Kong, D. S., Kim, H. K., Ha, J. H., Lee, M., Hong, J. I., & Jung, J. H.. Thermal stability and Young's modulus of mechanically exfoliated flexible mica. *Curr. Appl. Phys.* **18**, 1486-1491 (2018).

98. May, P., Khan, U., & Coleman, J.N. Reinforcement of metal with liquid-exfoliated inorganic nano-platelets. *Appl. Phys. Lett.* **103**, 163106 (2013).

99. Pan, Y., Wen, M., Wang, L., Wang, X., Lin, Y. H., & Guan, W. M. Iridium concentration driving the mechanical properties of iridium–aluminum compounds. *J. Alloys Compd.* **648**, 771-777 (2015).

100. Material: silicon (Si), bulk https://www.memsnet.org/material/siliconsibulk/ (Accessed: 30th July 2023)

101. Zhang, S. X., Liu, J., Zeng, J., Hu, P. P., & Zhai, P. F. Structural modification in swift heavy ion irradiated muscovite mica. *Chin. Phys. B* **26**, 106102 (2017).

102. Mukhopadhyay, T., Mahata, A., Adhikari, S.& Zaeem, M.A. Effective elastic properties of two dimensional multiplanar hexagonal nanostructures. *2D Mater.* **4**, 025006 (2017).
103. Ma, C., Chen, Y. & Arnold, W. Detection of subsurface cavity structures using contact-resonance atomic force microscopy *J. Appl. Phys.* **121**, 154301 (2017).
104. Rahman Rano, B., Syed, I. M. & Naqib, S. H. Elastic, electronic, bonding, and optical properties of WTe2 Weyl semimetal: a comparative investigation with MoTe2 from first principles. *Results Phys.* **19**, 103639 (2020).
105. Zeng, F., Zhang, W.B. & Tang, B.Y. Electronic structures and elastic properties of monolayer and bilayer transition metal dichalcogenides MX2 (M= Mo, W; X= O, S, Se, Te): a comparative first-principles study. *Chin. Phys. B* **24**, 097103 (2015).
106. Properties: iridium - properties and applications https://www.azom.com/properties.aspx?ArticleID=1700 (Accessed: 30th July 2023)
107. Falin, A., Cai, Q., Santos, E. J., Scullion, D., Qian, D., Zhang, R., Yang, Z., Huang, S., Watanabe, K., Taniguchi, T., Barnett, M.R., Chen, Y., Ruoff, R.S. & Li, L. H.. Mechanical properties of atomically thin boron nitride and the role of interlayer interactions. *Nature Commun.* **8**, 15815 (2017).
108. Drelich, J. A. R. O. S. L. A. W., Tormoen, G. W., & Beach, E. R. Determination of solid surface tension at the nanoscale using atomic force microscopy. *Contact Angle, Wettability and Adhesion* **4**, 237-264 (2006).
109. Peng, Q. & De, S. Outstanding mechanical properties of monolayer MoS2 and its application in elastic energy storage. *Phys. Chem. Chem. Phys.* **15**, 19427–19437 (2013).
110. Zhang, D., Ren, W., Wang, K., Chen, S., Zhang, L., Ni, Y., & Zhang, G. A thermal conductivity switch via the reversible 2H-1T′ phase transition in monolayer $MoTe_2$. *Chin. Phys. B* **32**, 050505 (2023).
111. Poisson's Ratio. Available at: https://polymerdatabase.com/polymer physics/Poisson Table.html. (Accessed: 30th July 2023)
112. Woo, S., Park, H. C. & Son, Y. W. Poisson's ratio in layered two-dimensional crystals. *Phys. Rev. B* **93**, 075420 (2016).
113. Castellanos-Gomez, A., Poot, M., Steele, G. A., Van Der Zant, H. S., Agraït, N., & Rubio-Bollinger, G. Elastic properties of freely suspended MoS2 nanosheets. *Adv. Mater.* **24**, 772–775 (2012).
114. Akhter, M. J., Kuś, W., Mrozek, A., & Burczyński, T. Mechanical properties of monolayer MoS2 with randomly distributed defects. *Materials* **13**, 1307 (2020).

115. Shen, J., Zhang, D., Zhang, F.-H. & Gan, Y. AFM tip-sample convolution effects for cylinder protrusions. *Appl. Surf. Sci.* **422**, 482–491 (2017).

116. Payam, A. F. Modeling and analysis of the capillary force for interactions of different tip/substrate in AFM based on the energy method. *ACS Meas. Sci. Au* (2023)

117. Bergström, L. Hamaker constants of inorganic materials. *Adv. Colloid Interface Sci.* **70,** 125-169 (1997).

118. Leite, F. L., Bueno, C. C., Da Róz, A. L., Ziemath, E. C. & Oliveira, O. N. Theoretical models for surface forces and adhesion and their measurement using atomic force microscopy. *Int. J. Mol. Sci.* **13**, 12773-12856 (2012).

119. Fernández-Varea, J. M. & Garcia-Molina, R. Hamaker constants of systems involving water obtained from a dielectric function that fulfills the f sum rule. *J. Colloid Interface Sci.* **231**, 394-397 (2000).

120. Ackler, H.D., French, R.H. & Chiang, Y.M. Comparisons of Hamaker constants for ceramic systems with intervening vacuum or water: from force laws and physical properties. *J. Colloid Interface Sci.* **179**, 460-469 (1996).

121. Lomboy, G., Sundararajan, S., Wang, K. & Subramaniam, S. A test method for determining adhesion forces and Hamaker constants of cementitious materials using atomic force microscopy. *Cem. Concr. Res.* **41**, 1157-1166 (2011).

122. Kozbial, A., Gong, X., Liu, H. & Li, L. Understanding the intrinsic water wettability of molybdenum disulfide (MoS_2). *Langmuir* **31**, 8429-8435 (2015).

123. Zhang, H., Ma, Y., Wan, Y., Rong, X., Xie, Z., Wang, W., & Dai, L. Measuring the refractive index of highly crystalline monolayer MoS_2 with high confidence. *Sci. Rep.* **5**, 8440 (2015).

124. Refractive index database. Available at: https://refractiveindex.info/?shelf=organic&book=poly%28methyl_methacrylate%29&page=Szczurowski. (Accessed: 30th July 2023)

125. Song, H., Gu, H., Fang, M., Chen, X., Jiang, H., Wang, R., Zhai, T., Ho, Y.T. & Liu, S. Layer-dependent dielectric function of wafer-scale 2D MoS_2. *Adv. Optical Mater.* **7**, 1801250 (2019).

126. Snapp, P., Kim, J. M., Cho, C., Leem, J., Haque, M. F., & Nam, S. Interaction of 2D materials with liquids: wettability, electrochemical properties, friction, and emerging directions. *NPG Asia Mater.* **12**, 22 (2020).

127. Fatima, S., Quadri, S. N., Parveen, S., Beg, S., Rahman, M., Ahmad, F. J., & Abdin, M. Z. Polymeric nanoparticles for potential drug delivery applications in cancer. In *Nanoformulation Strategies for Cancer Treatment.* (Elsevier, Amsterdam, 2021).

128. Maiti, A. & Pandey, A. Polymer and waste plastic in membranes. In *Materials science and materials engineering*; (Elsevier, Amsterdam, 2021).

129. Obi, B. *Polymeric foams structure-property-performance: a design guide*. (William Andrew, Oxford, 2017).

130. Aragones, J. L., MacDowell, L. G. & Vega, C. Dielectric constant of ices and water: a lesson about water interactions. *J. Phys. Chem. A* **115**, 5745-5758 (2011).

131. Strazdaite, S., Versluis, J., Backus, E. H. G. & Bakker, H. J. Enhanced ordering of water at hydrophobic surfaces. *J. Chem. Phys.* **140**, 054711 (2014).

132. Seo, Y., Jhe, W., Katan, A. J., Van Es, M. H. & Oosterkamp, T. H. Quantitative force versus distance measurements in amplitude modulation AFM: a novel force inversion technique. *Nanotechnol.* **20**, 9 (2009).

133. Sader, J. E., Uchihashi, T., Higgins, M. J., Farrell, A., Nakayama, Y., & Jarvis, S. P. Quantitative force measurements using frequency modulation atomic force microscopy—theoretical foundations. *Nanotechnol.* **16**, S94 (2005).

134. Boer-Duchemin, E., Tranvouez, E., & Dujardin, G. The interaction of an atomic force microscope tip with a nano-object: a model for determining the lateral force. *Nanotechnol.* **21**, 455704 (2010).

135. Matei, G. A., Thoreson, E. J., Pratt, J. R., Newell, D. B., & Burnham, N. A. Precision and accuracy of thermal calibration of atomic force microscopy cantilevers. *Rev Sci Instrum* **77**, 83703 (2006).

136. Clifford, C. A., & Seah, M. P. The determination of atomic force microscope cantilever spring constants via dimensional methods for nanomechanical analysis. *Nanotechnol.* **16**, 1666 (2005).

137. Yacoot, A. & Koenders, L. Aspects of scanning force microscope probes and their effects on dimensional measurement. *J. Phys. D. Appl. Phys.* **41**, 103001 (2008).

138. Cafolla, C., Payam, A. F. & Voïtchovsky, K. A non-destructive method to calibrate the torsional spring constant of atomic force microscope cantilevers in viscous environments *J. Appl. Phys* **124**, 154502 (2018).

139. Han, B., Key, B., Lapidus, S. H., Garcia, J. C., Iddir, H., Vaughey, J. T., & Dogan, F. From coating to dopant: how the transition metal composition affects alumina coatings on Ni-rich cathodes. *ACS Appl. Mater. Interfaces* **9**, 41291-41302 (2017).

140. Mandracci, P., Mussano, F., Rivolo, P. & Carossa, S. Surface treatments and functional coatings for biocompatibility improvement and bacterial adhesion reduction in dental implantology. *Coatings* **6**, 7 (2016).

141. Ma, Y., Guo, Q., Yang, M., Wang, Y., Chen, T., Chen, Q., Zhu, X., Xia, Q., Li, S. & Xia, H. Highly doped graphene with multi-dopants for high-capacity and ultrastable sodium-ion batteries. *Energy Storage Mater.* **13**, 134-141 (2018).

142. Liu, Y., Huang, Y. & Duan, X. van der Waals integration before and beyond two-dimensional materials. *Nature* **567**, 323–333 (2019).

143. Butt, H.-J. & Jaschke, M. Calculation of thermal noise in atomic force microscopy. *Nanotechnol.* **6**, 1 (1995).

144. Snopok, B., Laroussi, A., Cafolla, C., Voïtchovsky, K., Snopok, T., & Mirsky, V. M. Gold surface cleaning by etching polishing: Optimization of polycrystalline film topography and surface functionality for biosensing. *Surf. Interfaces* **22**, 100818 (2021).

145. Bonaccurso, E., Kappl, M. & Butt, H. J. Thin liquid films studied by atomic force microscopy. *Curr. Opin. Colloid Interface Sci.* **13**, 107-119 (2008).

146. Wu, W., Chen, Z., Cheng, X. & Wang, Y. EBSD study of (110) orientation of iridium (Ir) coating on niobium (Nb) substrate by double glow plasma. *Nucl. Instruments Methods Phys. Res. Sect. B Beam Interact. with Mater. Atoms* **307**, 315–319 (2013).

147. Voïtchovsky, K., Kuna, J. J., Sonia Antoranz Contera, E. T. & Stellacci, F. Direct mapping of the solid–liquid adhesion energy with subnanometre resolution. *Nat. Nanotechnol.* **5**, 401-405 (2010).